RSC Advances

PAPER

Check for updates

Cite this: *RSC Adv.*, 2020, **10**, 44920

A new cobalt(II) *meso*-porphyrin: synthesis, characterization, electric properties and application in the catalytic degradation of dyes†

Nesrine Amiri,*[a] Mouhieddinne Guergueb,[a] Maged S. Al-Fakeh,[b] Marwa Bourguiba[cd] and Habib Nasri[a]

Received 15th October 2020
Accepted 22nd November 2020

DOI: 10.1039/d0ra08786f

rsc.li/rsc-advances

In this work, a new porphyrin, 5,10,15,20-tetrakis{4-[((4-methoxyphenyl)acetyl)oxy]phenyl}porphyrin (H_2TMAPP) (**1**), and its cobalt complex [Co^{II}(TMAPP)] (**2**) were synthesized in good and quantitative yields, respectively. The chemical structures of these synthesized compounds were confirmed by FT-IR, ^{1}H NMR, MS, UV-visible, and fluorescence spectroscopy. Their photophysical properties, namely their molar extinction coefficients ($\sum$), fluorescence quantum yields (Φ_f) and lifetimes (τ_f), were determined and compared with those of *meso*-tetraphenylporphyrin. Furthermore, their electrochemical behaviours were examined using cyclic voltammetry (CV). Dielectric properties such as the conductivity (σ) and the real (M') and imaginary (M'') parts of the dielectric modulus were investigated as a function of temperature and frequency. The impedance analysis was carried out using Cole–Cole plots to elucidate the electrical conduction mechanism. The catalytic power and the adsorption properties of the prepared compounds were studied for methylene blue (MB) and crystal violet (CV) degradation. The results reveal that the studied compound [Co^{II}(TMAPP)] can be used as a catalyst for the decolourisation of dyes in the presence of H_2O_2.

1. Introduction

Porphyrin, which is a large, widely conjugated cyclic planar molecule, is attracting the attention of many researchers in various fields due to its remarkable photochemical, electrochemical, and biochemical properties.[1] The synthesis and functionalization of this macrocycle have long been of interest because of the potential of porphyrin derivatives in diverse fields, such as catalysis, photocatalysis, molecular wires,[2–4] sensitive reagents in photodynamic therapy (PDT) for tumors and cancers,[5] functional dyes and pigments,[6] solar cells,[7] energy transfer, and light-harvesting.[8–11] The substitution of suitable organic groups on the periphery of porphyrin rings as well as the coordination of the metal in the center of the porphyrin ring permit the design of new synthetic porphyrins. Substitution at the *meso* positions of highly aromatic and bulky groups, such as naphthyl, phenanthryl, or pyrenyl porphyrins, has been reported, which alters its aromatic character. The development of ester functions with porphyrins has attracted much attention due to their wide range of applications.[12–14] For example, Carminati *et al.*[13] described the preparation of an iron porphyrin substituted at the *meso* position by amino ester groups. These complexes are emerging as candidates in catalysis measurements. Meden F. Isaac *et al.*[14] described the preparation of novel porphyrin dimers bearing ester groups in the *meso* position. These compounds have potential applications in binary cancer therapies. In another example, Olycen Oviedo *et al.*[12] synthesized *meso*-tetra-(4-benzoate-9-phenanthryl)-porphyrin and its Zn and Cu complexes, which have been studied both in the photosensitized oxidation of phenols and photoinduced antibacterial efficiency. In addition, the development of methoxyphenyl functions with porphyrins has been the subject of particular attention due to their catalytic activities, *i.e.* they have been used as catalysts for biomimetic oxidation[15,16] and for the degradation of green dye.[17] Recently, our research group managed to design and characterize new metalloporphyrin-based materials.[18–20] In this paper, and in continuation of our work on the functionalization of *meso* tetra-arylporphyrins, we have synthesised a new porphyrin, H_2TMAPP (**1**) (TMAPP = 5,10,15,20-tetrakis{4-[((4-methoxyphenyl)acetyl)oxy]phenyl} porphyrin), and its cobalt complex [Co^{II}(TMAPP)] (**2**), which are substituted at the *meso* position by ester groups comprising two benzene rings plus methoxy functions (Scheme 1). With this aim, our compounds have been characterized by infrared,

[a]*Laboratory of Physico-Chemistry of Materials, University of Monastir, Avenue of the Environment, 5019 Monastir, Tunisia. E-mail: nesamiri@gmail.com; Tel: +216 28256432*

[b]*Department of Chemistry, Faculty of Science, Qassim University, Saudi Arabia*

[c]*Applied Mechanics and Systems Research Laboratory (LASMAP-EPT), Polytechnic School, University of Carthage, La Marsa, Tunisia*

[d]*Faculty of Science of Tunis, University of Tunis El Manar, Tunisia*

† Electronic supplementary information (ESI) available. See DOI: 10.1039/d0ra08786f

This article is licensed under a Creative Commons Attribution 3.0 Unported Licence.

This journal is © The Royal Society of Chemistry 2020

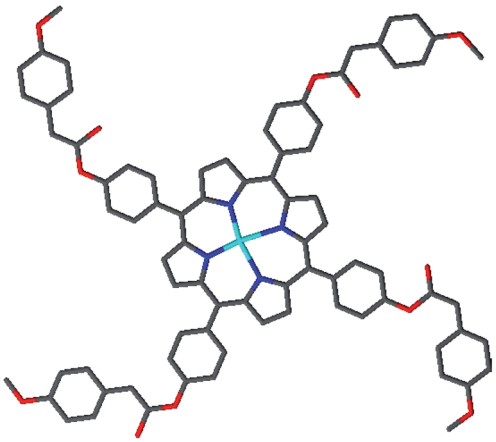

Scheme 1 Molecular structure of *meso*-tetrakis{4-[((4-methoxyphenyl)acetyl)oxy]phenyl} porphyrinato cobalt(II) (**2**) (drawing of the molecule).

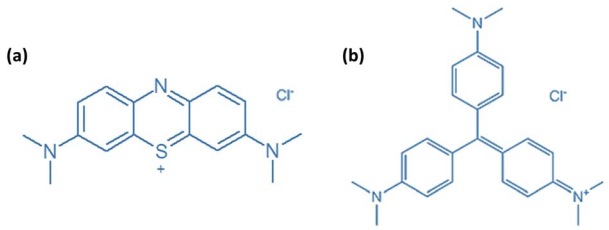

Scheme 2 Molecular structures of (a) methylene blue (MB) and (b) crystal violet (CV).

proton nuclear magnetic resonance spectroscopy, mass spectrometry, and elemental analysis. We also report on their optical and electrochemical properties. Therefore, in this work, attention has been focused on the investigation of the conductivity (σ) and the real (M') and imaginary (M'') parts of the dielectric modulus as a function of frequency and temperature of Co(II)-porphyrin to obtain the maximum amount of information from the experimental data. The impedance (Z) was also investigated. Further, their dye adsorption properties and catalytic degradation using methylene blue (MB) and crystal violet (CV) dyes (Scheme 2) were evaluated.

2. Experimental

2.1. General

All solvents and reagents were purchased from Sigma Aldrich or ACROS ORGANICS. Used solvents were purified using the available literature methods.[21] Silica gel 150 (35–70 μm particle size, Davisil) was used for final purification of the products. Double distilled water was used in the experiments. The starting material, the aldehyde 4-formylphenyl(4-methoxyphenyl) acetate, was prepared as previously described.[22] The macrocycle of H_2TMAPP was synthesized and purified according to the procedures described by Lindsey *et al.*,[23] and cobalt was inserted into the porphyrin molecule by the dimethylformamide method[24,25] (Scheme S1†).

2.2. Synthesis

Synthesis of 4-formylphenyl (4-methoxyphenyl)acetate. 4-Methoxyphenylacetic acid (6 g, 0.036 mol), 4-hydroxybenzaldehyde (4.4 g, 0.036 mol), and dimethylaminopyridine (DMAP, 0.5 g, 0.0036 mol.) were dissolved in dichloromethane (20 mL) at 0 °C. To this solution, *N*,*N'*-dicyclohexylcarbodiimide (DCC) (7.5 g, 0.036 mol) in dichloromethane (25 mL) was added dropwise, and the mixture was stirred at 0 °C and then at room temperature for 12 h. Upon completion of the reaction, the mixture was filtered, and dichloromethane was removed by rotary evaporation. The solution was poured into water, and the solid was collected by filtration, washed with water followed by hexanes, and dried under vacuum to afford a pale-yellow powder (9 g, yield 92.5%). Anal. Calcd. For $C_{16}H_{14}O_4$ (270.28): C 71.04, H 5.22%; found C 71.26, H 5.34%. ^{1}H NMR ($CDCl_3$, 300 MHz): δ = 9.98 (s, 1H), 7.95 (d, J = 6.4 Hz, 2H), 7.32 (d, J = 8.7 Hz, 4H), 6.92 (d, J = 7.7 Hz, 2H), 3.90 (s, 3H), 3.75 (s, 2H) ppm. ^{13}C NMR ($CDCl_3$, 300 MHz): δ = 191.73 (C=O of CHO), 163.68 (C=O of ester), 54.97 (C–O of methoxy), 158.69, 155.04, 131.39, 130.72, 122.37 ppm.

Synthesis of the *meso*-tetrakis{4-[((4-methoxyphenyl)acetyl)oxy]phenyl}porphyrin (H_2TMAPP) (1). 4-Formylphenyl (4-methoxyphenyl)acetate (500 mg, 1.85 mmol), and pyrrole (127 μL, 1.85 mmol) were added to distilled chloroform (300 mL) in a double necked round bottom flask under argon and shielded from light. Boron trifluoride diethyl etherate, $BF_3 \cdot OEt_2$ (192.4 μL) was added, and the reaction was maintained at room temperature for two hours. Two pipettes of triethylamine and 0.75 equivalents of *p*-chloranil (179.2 mg, 1.66 mmol) were added, and the solution was heated to reflux (light protection was removed). After 1 hour, the obtained solution was cooled to room temperature. The solvent was evaporated and the residue was filtered over silica with $CHCl_3$/hexane (1 : 9). The expected compound was obtained as a purple solid (yield 69%). ^{1}H NMR [DMSO-d_6, 300 MHz] δ(ppm): 8.83 (s, 8H, H_β-pyrrol), 8.23 (d, J = 7.4 Hz, 8H), 7.56 (d, J = 7.5 Hz, 8H), 7.44 (d, J = 7.5 Hz, 8H), 7.02 (d, J = 7.5 Hz, 8H), 4.06 (s, 8H), 3.81 (s, 12H), −2.88 (s, 2H, hpyrrol). UV/vis [λ_{max} (nm) in CH_2Cl_2, (log ε)]: 425 (5.92), 522 (5.67), 550 (4.32), 597 (4.15), 653 (3.98). MS [ESI]: *m*/*z* calcd for $C_{80}H_{62}N_4O_{12}$: 1271.36 found: 1272.36. Anal. calcd for $C_{80}H_{62}N_4O_{12}$: C 75.51, H 4.87, N 4.40%; found: C 75.77, H 4.56, N 4.42%. FTR-IR cm^{-1}: 3323 (ν_{NH} porphyrin), 2897 (ν_{CH} porphyrin), 1736 ($\nu_{C=O}$ ester), 1285 (ν_{C-O} ester), 1225 (ν_{O-C} methoxy), 987 (δ_{CCH} porphyrin).

Synthesis of the *meso*-tetrakis{4-[((4-methoxyphenyl)acetyl)oxy]phenyl} porphyrinato cobalt(II) complex [Co^{II}(TMAPP)] (2). H_2TMAPP (0.4 g, 0.314 mmol) was dissolved in DMF (150 mL). The solution was heated under reflux with magnetic stirring. Upon dissolution of the H_2TMAPP, $CoCl_2 \cdot 6H_2O$ (1 g, 4.2 mmol) was added. The reaction mixture was stirred for 2 hours. Thin-layer chromatography (alumina, using CH_2Cl_2 as eluant) indicated no free base porphyrins at this point. After that, the solution was cooled to 50–60 °C, and H_2O (50 mL) was added to it. The obtained solid was filtered and washed with hexane. The resulting product was vacuum-dried to afford 66% yield of [Co^{II}(TMAPP)]. ^{1}H NMR [DMSO-d_6, 300 MHz] δ(ppm): 15.69 (s,

8H, H_{β}-pyrrol), 9.25 (d, $J = 7.5$ Hz, 8H), 8.81 (d, $J = 7.8$ Hz, 8H), 8.49 (d, $J = 7.7$ Hz, 8H), 7.75 (d, $J = 7.5$ Hz, 8H), 4.12 (s, 8H), 3.89 (s, 12H). UV/vis [λ_{max} (nm) in CH_2Cl_2, (log ε)]: 415 (5.85), 539 (5.49). MS [ESI]: m/z calcd for $C_{80}H_{60}CoN_4O_{12}$: 1328.28, found: 1329.29. Anal. calcd for $C_{80}H_{60}CoN_4O_{12}$: C 72.27, H 4.52, N 4.22%; found: C 72.34, H 4.23, N 4.07%. FTR-IR cm^{-1}: 2923 (ν_{CH} porphyrin), 1737 ($\nu_{C=O}$ ester), 1260 (ν_{C-O} ester), 1226 (ν_{O-C} methoxy), 993 (δ_{CCH} porphyrin).

2.3. Instrumentation

IR and ^{1}H NMR spectroscopy. IR and ^{1}H NMR spectra were recorded on a Nicolet Impact 410 and a Bruker AVANCE (300 MHz) spectrometer, respectively. ^{1}H NMR measurements were carried out at room temperature.

Mass spectral studies. A Thermo Scientific "Q Exactive" mass spectrometer was operated under electrospray ionization (ESI) in positive mode with the following settings: accelerating voltage 20 kV, grid voltage 62% of the accelerating voltage, extraction delay time of 100 ns.

Optical measurements. UV-vis spectra of H_2TMAPP and [Co^{II}(TMAPP)] were measured with a Varian Cary 5000 spectrophotometer in CH_2Cl_2 solution at concentrations of *ca.* 10^{-6} M. The two samples were characterized to see the displacement of the Soret band. From these spectra, the molar extinction coefficient, ε, of the Soret band and secondary bands were calculated. A Varian Cary Eclipse luminescence spectrofluorometer was used to obtain emission spectra in dichloromethane at room temperature, and the fluorescence quantum yield (Φ_f) was measured using the following equation:[26,27]

$$\Phi_f/\Phi_r = (A_r/A_f)(F_f/F_r)(n_f^2/n_r^2) \quad (1)$$

In this relation, Φ_r, A_r, F_r and n_r are the fluorescence quantum efficiency, absorbance at excitation wavelength, emission integration area, and refractive index for the reference, while Φ_f, A_f, F_f and n_f are those of the tested porphyrinic species. [Zn^{II}(TPP)] was used as reference with the standard quantum yield of $\Phi_f = 0.03$.[28]

Electrochemical analysis. Cyclic voltammetry (CV) experiments were performed with a CH-660B potentiostat (CH Instruments). All analytical experiments were conducted at room temperature under an argon atmosphere (argon stream) in a standard one-compartment, three-electrode electrochemical cell. Tetra-*n*-butylammonium perchlorate (TBAP) was used as the supporting electrolyte (0.2 M) in dichloromethane previously distilled over calcium hydride under argon. An automatic ohmic drop compensation procedure was systematically implemented before the CV data were recorded with electrolytic solutions containing the studied compounds at concentrations of *ca.* 10^{-3} M. CH Instruments vitreous carbon ($\Phi = 3$ mm) working electrodes were polished with 1 μm diamond paste before each recording. The $Ag/AgNO_3$ 0.01 M (TBAP 0.2 in CH_2Cl_2) redox couple was used as the reference electrode. The potential of the ferrocene/ferrocenium redox couple was used as an internal reference (86 mV *vs.* $Ag/AgNO_3$ under our experimental conditions). For comparison with previously published data, all potentials given in the text and in Table S2† have been converted to values relative to the saturated calomel electrode (SCE) by using the following relationship: E(SCE) = E($Ag/AgNO_3$) + 298 mV.[29]

Adsorption experiments. The adsorption of methylene blue (MB) and crystal violet (CV) (Scheme 2) in the presence of H_2TMAPP and [Co^{II}(TMAPP)] was carried out in batch mode with constant agitation. Kinetic experiments were studied by stirring a series of flasks enclosing 5 mL of methylene blue solution with 3 mg of adsorbent with the same stirring speed. After the required time was reached, the supernatant liquid was filtered. The concentration of methylene blue was measured at 664 nm and that of crystal violet was measured at 591 nm.

Catalytic degradation of methylene blue and crystal violet. Two different organic dye pollutants, namely, methylene blue (MB) and crystal violet (CV), were chosen to investigate the catalytic activity of [Co^{II}(TMAPP)] (**2**). In a typical experiment, to a 10 mL aqueous solution of dye (30 mg L^{-1}) was added 1 mL of H_2O_2 (30 wt%) and 3 mg of [Co^{II}(TMAPP)] (**2**). Then, a preferred amount of catalyst was added to this mixture at an agitation speed of 150 rpm. The reaction solution was pipetted into a quartz cell and its absorption spectrum was measured for different reaction times using an UV-visible spectrophotometer. Blank experiments were also conducted to confirm that the reactions did not proceed with catalyst in the absence of H_2O_2 or without catalyst in the presence of H_2O_2.

3. Results and discussion

3.1. IR and ^{1}H NMR spectroscopies

In order to gain more insights into the structures of the porphyrin and metalloporphyrin, detailed IR and ^{1}H NMR studies were performed. Representative solid-state infrared spectra are shown in Fig. S1 and S2.† The spectra of the free porphyrin H_2TMAPP and metalloporphyrin [Co^{II}(TMAPP)] were very similar, and only minor frequency shifts were observed. The only obvious difference arose from the disappearance of the N–H (3323 cm^{-1}) vibration frequency of free base porphyrin, indicating the formation of cobalt(II) porphyrin compound (Fig. S2†). Our compounds are in general agreement with those recently reported for a number of porphyrins.[19,28] The 2897 and 2923 cm^{-1} peaks are associated with antisymmetric and symmetric alkyl C–H vibrations. The strongest absorption peaks in the spectra at 1736 and 1260 cm^{-1} can be associated with the ester group stretch. The bands observed around 1000 cm^{-1} are assigned to δ(CCH) vibration modes for the *meso*-porphyrin. The ^{1}H NMR spectra of **1** and its Co(II) derivative **2** were recorded in deuterated chloroform at 298 K (Fig. S3 and S4†). The free base porphyrin shows characteristic inner amino proton (NH) signals at −2.88 ppm which are absent in metalloporphyrin. The β-pyrrole protons resonate as a singlet at 8.83 ppm, and the aromatic protons of the *meso*-phenyl rings resonate in the range of 8.24–7.00 ppm, which corresponds to a classical case for all *meso*-porphyrins. The methyl and methoxy protons of *para*-methoxy phenolate appear at 4.06 and 3.81 ppm, respectively. [Co^{II}(TMAPP)] in $CDCl_3$ has paramagnetic properties, as shown by the chemical shifts and the

 This journal is © The Royal Society of Chemistry 2020

broadened singlets of the H_β-pyrrolic protons (at 15.69 ppm).[30] This property is due to the 3d configuration of cobalt(II).

3.2. Mass spectral studies

Mass spectroscopy is widely used in the study of porphyrins to determine the molecular weights of porphyrins and metalloporphyrins by ESI-mass spectroscopic techniques in the positive ion mode. The molecular spectra of compounds **1** and **2** (Fig. S5 and S6†) are best recorded at the lowest possible temperature. These mass spectra show the molecular ion peaks of these compounds, which are in good agreement with the structures suggested by elemental analysis and spectral studies. The protonated molecular ion peaks, [M] or [M + H], of H_2TMAPP were observed at 1271.36 (Fig. S5†). In the MALDITOF mass spectrum of the cobalt porphyrin, a molecular ion peak was observed at 1328.29 (Fig. S6†). These mass values overlapped with the theoretically calculated mass values for the [M] or [M + H] of the two compounds.

3.3. Optical properties

UV-vis absorption spectroscopy. Fig. 1 shows the UV-visible spectrum of the demetallated macrocycle H_2TMAPP compared with the response of the metallated macrocycle [Co^{II}(TMAPP)]. The ground state electronic absorption spectra of the porphyrins are characterized by an intense band called the Soret or B band at around 400 nm. The Soret band of H_2TMAPP was observed at 425 nm (log ε = 5.92) (Table S1†), while the four Q bands, decreasing in intensity, were at 522 nm (log ε = 5.67), 550 nm (log ε = 4.32), 597 nm (log ε = 4.15) and 653 nm (log ε = 3.98) (Fig. 1). The Q bands decreased in intensity in the following order: $Q_y(1,0) > Q_y(0,0) > Q_x(1,0) > Q_x(0,0)$. These absorption bands are characteristic for porphyrins and are due to the $a_{1u}(\pi) - e_g(\pi^*)$ and $a_{2u}(\pi) - e_g(\pi^*)$ transitions for the Soret and Q bands, respectively.[31,32] The four Q-bands of the metal-free precursor collapsed into one Q band following metalation, confirming the successful insertion of cobalt as a central metal. The Q band of [Co^{II}(TMAPP)] was observed at 534 nm (log ε = 5.49), while the Soret band was observed at 415 nm (log ε = 5.85), as shown in Fig. 1 (Table S1†), showing that there is a 10 nm blue shift for [Co^{II}(TMAPP)] compared to H_2TMAPP. This blue shift is a result of the insertion of the central metal and generates an increase of the symmetry (from D_{2h} to D_{4h}), and the introduction of a heavy metal such as cobalt could result in an increase in the degree of perturbation and electron delocalisation within the porphyrin macrocycle.

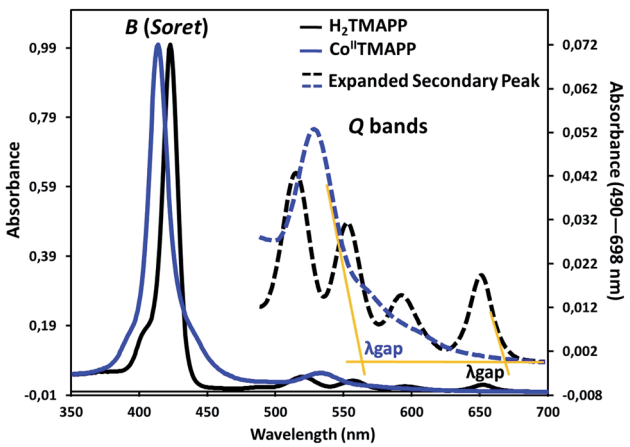

Fig. 1 UV-vis absorption spectra of H_2TMAPP and [Co^{II}(TMAPP)] in CH_2Cl_2 solutions at concentrations around 10^{-6} mol L^{-1}.

The optical band gap ($E_{g\text{-op}}$), which corresponds to the energy difference between the levels of the HOMO and LUMO, was obtained from the UV-visible spectra. This energy was calculated from the value of the tangent to the Q(0,0) absorption band (λ_{gap}). The $E_{g\text{-op}}$ values were 1.85 eV (λ_{gap} = 670 nm) for H_2TMAPP and 2.18 eV (λ_{gap} = 568 nm) for [Co^{II}(TMAPP)], which are in the normal range of *meso*-porphyrins and magnesium metalloporphyrins.[19,33,34]

Steady-state emission spectroscopy. The room temperature fluorescence spectra in dichloromethane (10^{-6} mol L^{-1}) are shown in Fig. 2. The fluorescence emission is attributed to the transition from the excited singlet state S_1/S_2 to the ground state S_0 ($S_2 \rightarrow S_0$, $S_1 \rightarrow S_0$). The fluorescence of the B (Soret) band is attributed to the transition from the second excited singlet state S_2 to the ground state S_0, $S_2 \rightarrow S_0$, and the Soret fluorescence is about 2 orders of magnitude weaker than that of the $S_1 \rightarrow S_0$ transition of the Q band emission. Upon excitation at 522 nm, the free base porphyrin displayed two emission peaks of $S_1 \rightarrow S_0$, centered at 655 nm and 719 nm (Fig. 2a). The spectrum of the metalloporphyrin [Co^{II}(TMAPP)] showed a very weak fluorescence band, and when excited at 540 nm, it gave two split emission bands at 653 nm (S_1 [Q(0,0)] $\rightarrow S_0$) and at 718 nm (S_1 [Q(0,1)] $\rightarrow S_0$) (Fig. 2b). It is noteworthy that the λ_{max} values of the Q(0,0) and Q(0,1) bands of these compounds are practically the same; the bands in the complex are similar to those in the free porphyrin but with a lower intensity (Fig. 2c). As previously reported, the decrease in the emission band intensity of compound **1** is probably due to the cobalt atom effect.[18,35–38] In the region of 350–700 nm, the excitation spectra were approximately mirror images of the absorption spectra, indicating that they correspond to a similar electron transition process (Fig. 2a and b). The fluorescence quantum yields (Φ_f) of the starting material H_2TMAPP and [Co^{II}(TMAPP)] were 0.050 and 0.028, respectively. The singlet excited-state lifetimes were measured by the single-photon counting technique, and the fluorescence decays of the starting material (**1**) and (**2**) species were fitted to single exponentials. The representative fluorescence decays (τ_f) of these two derivatives are presented in Fig. 2d. As expected, the τ_f values of the *meso*-porphyrin free bases (*ca.* 5.93 ns) are much higher than those of [Co^{II}(TMAPP)] (1.5 ns).

3.4. Electrochemical characterization

The cyclic voltammograms (CV) of the studied porphyrins in tetra-*n*-butylammonium perchlorate (TBAP) electrolyte (0.2 M) in the non-coordinating solvent CH_2Cl_2 under an argon atmosphere are displayed in Fig. 3, and all potential values are given in volts *versus* SCE. The free base H_2TMAPP exhibited two reversible one-electron reduction waves and three reversible

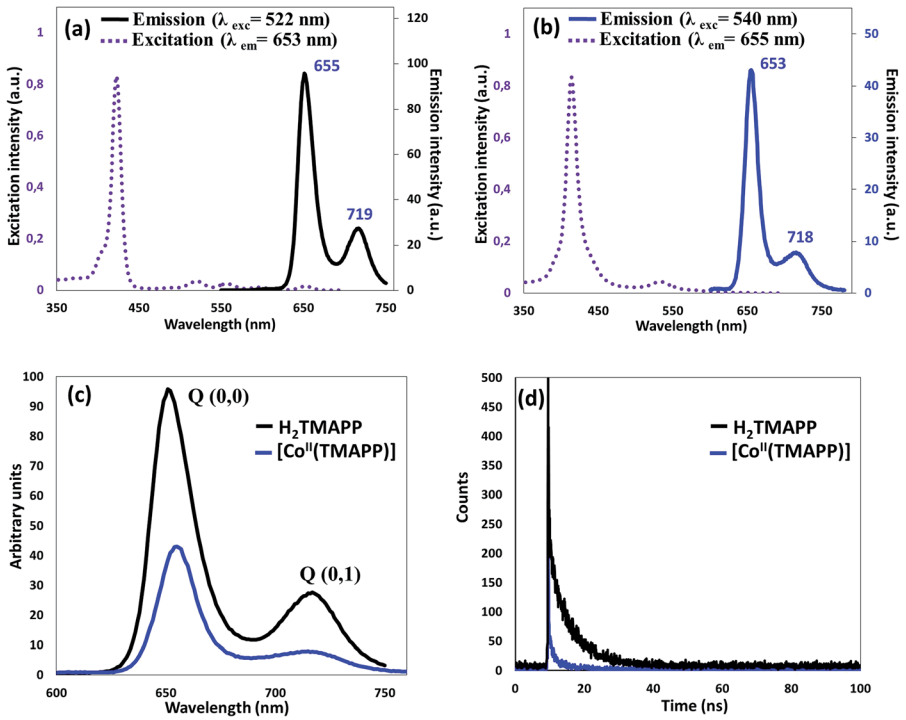

Fig. 2 (a) Excitation and emission spectra of H_2TMAPP, (b) excitation and emission spectra of [Co^{II}(TMAPP)], (c) emission spectrum of H_2TMAPP and [Co^{II}(TMAPP)] as 10^{-6} mol L^{-1} solutions in dichloromethane, (d) fluorescence decay profiles of (**1**) and (**2**).

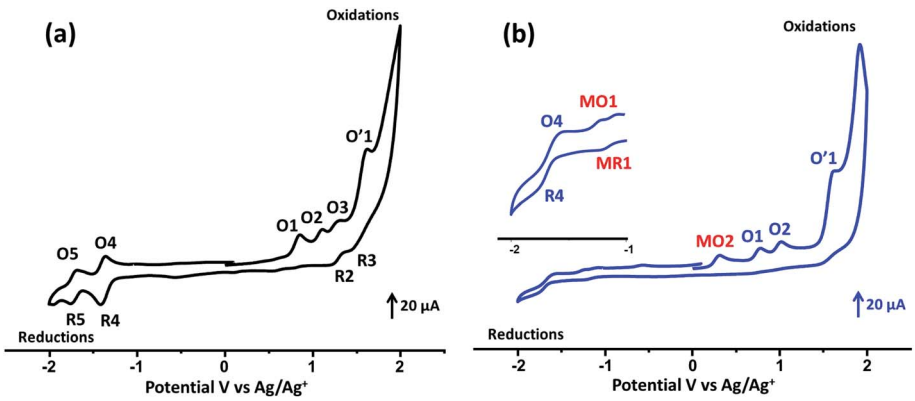

Fig. 3 Cyclic voltammograms of (a) H_2TMAPP and (b) [Co^{II}(TMAPP)] (the inset shows an enlarged view). The solvent was CH_2Cl_2, and the concentration was *ca.* 10^{-3} M in 0.2 M TBAP, 100 mV s^{-1}, vitreous carbon working electrode (Ø = 3 mm).

one-electron oxidation waves, which correspond to the reduction and the oxidation of the porphyrin ring, respectively (Fig. 3a). The values of the half-wave potentials were 1.15 (O1), 1.46 (O2, R2), and 1.66 (O3, R3) V for the first, second, and third oxidation waves, respectively. The $E_{1/2}$ values of the first and second reduction waves were −1.08 (R4, O4) and −1.41 (R5, O5) V, respectively. The $E_{1/2}$ values of H_2TMAPP are close to those of *meso*-porphyrin (Table S2†).[17,39] Concerning our Co(II)-TMAPP derivative (**2**), it presents three one-electron reversible oxidations (Fig. 3b), where the first corresponds to the center metal [Co(II)/Co(III)] (MO2) oxidation followed by two ring oxidations, with an E_{ap} (E_{ap} = anodic peak potential) value of 0.61 V; this is in the range of 0.60–0.98 V, which has been shown in several solvents for cobalt metalloporphyrins (Table S2†).[17,40–42] The reduction of the same [Co^{II}(TMAPP)] species leads to reduction of the centre metal [Co(II)/Co(I)] (with $E_{1/2}$ = −0.93 V (MR1, MO1)) followed by a second ring cantered one-electron reduction at quite negative potentials (with $E_{1/2}$ = −1.38 V (R4, O4)). Moreover, these two compounds exhibit an irreversible oxidation wave (O′1) with an E_{ap} value of 1.91 V, which can be attributed to oxidation of the phenyl rings of the *meso*-porphyrin.[43]

3.5. Complex impedance spectroscopy

Conductivity. Fig. 4 illustrates the variation of $\sigma(\omega)$ *vs.* $\ln(\omega)$ for [Co^{II}(TMAPP)] in the temperature range of 300–450 K. It is

 This journal is © The Royal Society of Chemistry 2020

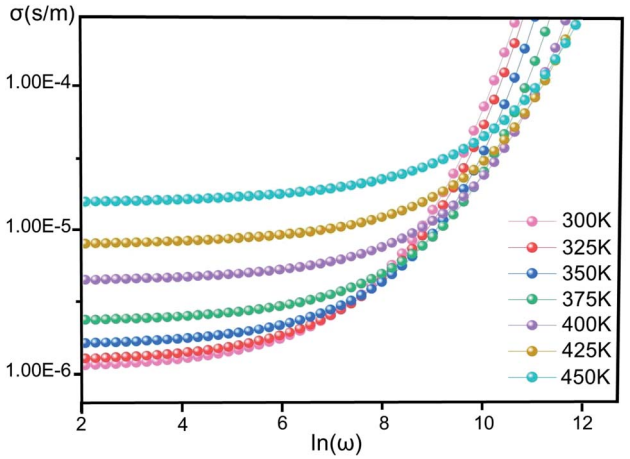

Fig. 4 The conductivity (σ) *versus* the frequency of [Co^{II}(TMAPP)] at various temperatures.

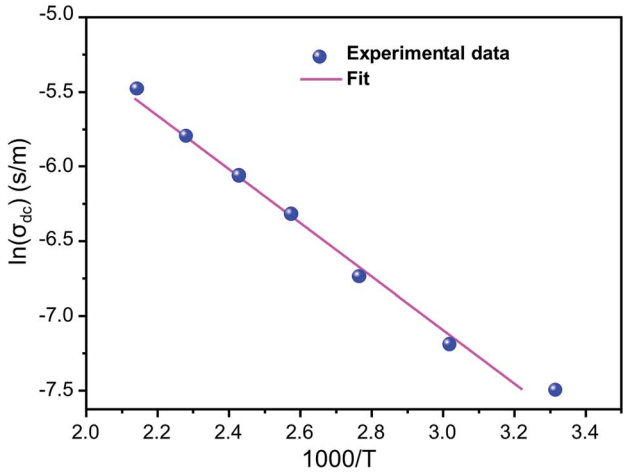

Fig. 5 Variation of ln(σ_{dc}) as a function of (1000/T).

clear that the frequency of $\sigma(\omega)$ remains constant at low frequency and after a certain frequency; it increases with the power law with increasing frequency. This behavior has also been observed in other organic compounds.[44–47] This behaviour confirms the result found by the complex impedance. The $\sigma(\omega)$ can be represented dynamically by the universal response (Jonscher power law) relation:[48]

$$\sigma(\omega,T) = \sigma_{dc}(T) + \sigma_{ac}(\omega,T) \quad (2)$$

where σ_{dc} is related to direct conduction (independent of frequency while temperature dependent) and σ_{ac} is related to relaxation or polarization conductivity (frequency dependent and weakly temperature dependent). The polarization conductivity is described by the relation:[49]

$$\sigma_{ac}(\omega,T) = A\omega^{s} \quad (3)$$

where A is a pre-exponential factor which depends on the temperature, ω ($=2\pi f$) is the angular frequency and the exponent s represents the degree of interaction between mobile ions and the lattice.

Fig. 5 shows ln(σ_{dc}) as a function of 1000/T. We note that ln(σ_{dc}) decreases linearly with increasing reciprocal temperature. This indicates that the dc conductivity is a thermally activated process. The temperature dependence of σ_{dc} can be represented by the usual Arrhenius relation:[50,51]

$$\sigma_{dc} = \sigma_0 \exp(-\Delta E_{dc}/k_B T) \quad (4)$$

where σ_0 is a constant that denotes the pre-exponential factor, ΔE_{dc} is the activation energy for the conduction process, k_B is Boltzmann's constant and T is the absolute temperature. The linear fit to this graph yields the activation energy ΔE_{as} 0.326 eV.

Complex impedance. The complex impedance is represented by the equation

$$Z^* = Z' - iZ'' \quad (5)$$

where Z' is the real part and Z'' is the imaginary part. Fig. 6 shows the impedance plots of Z'' with Z' at various temperatures for [Co^{II}(TMAPP)]. It can be observed that this spectrum at each temperature consists of a single well-shaped semicircle. Also, it can be seen that the diameters of the semicircles decrease when the temperature increases. This behaviour confirms the semiconducting characteristic of our compound in the entire explored temperature range. The radius is related to the defect states effect, which decreases with the applied voltage. These single semicircle impedance characteristics in the Cole–Cole plots can usually be reproduced with an equivalent circuit, as shown in the inset of Fig. 7. The equivalent circuit can be designed as a single parallel resistor (R_p) and capacitor (CPE) network with a series resistance (R_s).[52]

Modulus. The electrical modulus M^* is expressed as:[53]

$$M^*(\omega) = 1/\varepsilon^*(\omega) = M' + iM'' \quad (6)$$

where ε^* is the complex permittivity and M' and M'' are the real and the imaginary parts of the electric modulus, respectively.

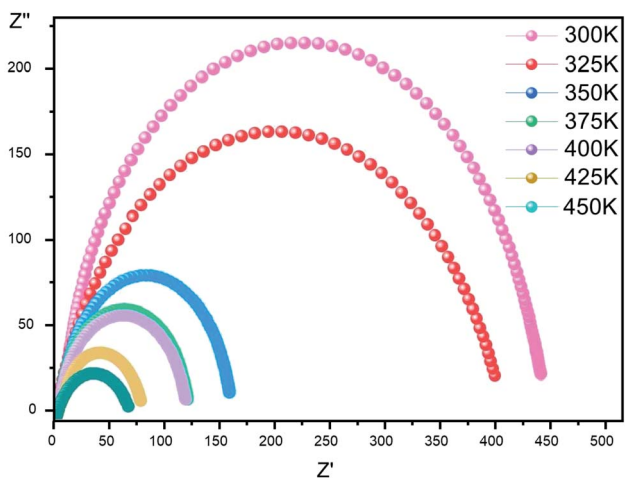

Fig. 6 Complex impedance plot spectra of [Co^{II}(TMAPP)] (**2**).

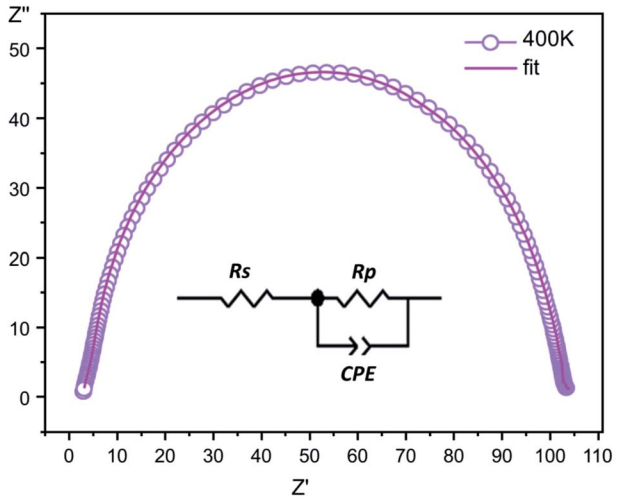

Fig. 7 The fitted circle on the experimental data at 400 K and the equivalent circuit.

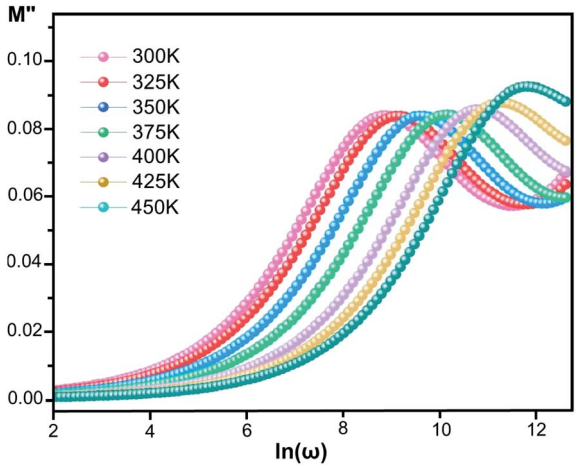

Fig. 9 Imaginary part of the electric modulus, M'', *versus* frequency at various temperatures for [Co^{II}(TMAPP)].

Fig. 8 and 9 show the frequency dependence of the real and imaginary parts of the electric modulus at various temperatures. In the lower frequency region, M' has low values or shows a tendency to zero in the overall range of temperature (Fig. 8), whereas it exhibits a maximum value in the high frequency region; this can be attributed to the enhancement of the conductivity because the charge carriers are mobile through a short distance. In addition, the values of M' were found to be near zero for all the given temperatures, which may be due to the suppression of electrode polarization. It can be also noted that M' decreases with increasing temperature over the entire range of frequency.[54–56] The plot of the imaginary part M'' as a function of frequency (Fig. 9) shows an asymmetric maximum at all measured temperatures. The position of the peak M''_{max} shifts to higher frequency as the temperature increases. Two apparent distinct regions were observed and are temperature dependent. The first is located towards the left of the peak, which is associated with a conduction process where the charge carriers are mobile. The other region towards the right of the peak is related to the relaxation polarization process, where the charge carriers are spatially confined to the potential wells.

The relaxation peak (M''_{max}) shifts with increasing temperature, which indicates that the temperature plays an effective role in decreasing the relaxation time τ. The corresponding relaxation time satisfies an almost linear dependence, in accordance with the Arrhenius law:[57]

$$\tau = \tau_0 \exp(\Delta E_\tau / k_B T) \tag{7}$$

where τ_0 is a constant characteristic relaxation time that represents the time of a single oscillation of a dipole in the potential well, ΔE_τ is the free energy of activation for dipole relaxation and τ ($\tau = 1/2\pi f_{max}$) represents the average or the most probable value of the spread of the relaxation time. The plot of ln τ *versus* 1000/T for the studied device is shown in Fig. 10. The value of the activation energy ΔE_τ was calculated from the slope and the intercept of the linear fit and was found to be 0.319 eV.

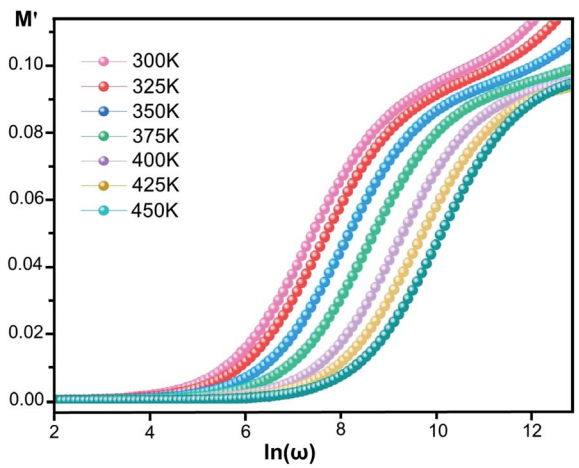

Fig. 8 Real part of the electric modulus, M', *versus* frequency at various temperatures for [Co^{II}(TMAPP)].

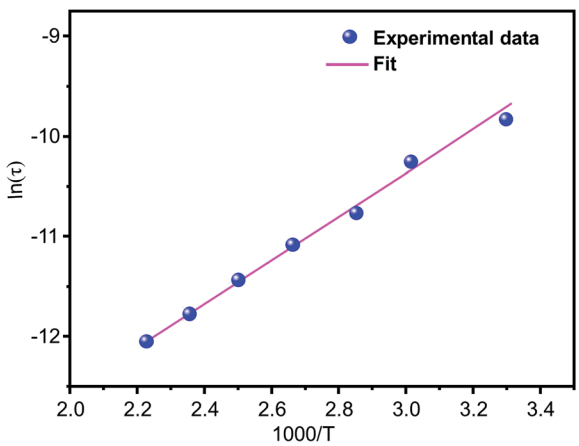

Fig. 10 The variation of the relaxation time (τ) with temperature.

 This journal is © The Royal Society of Chemistry 2020

The activation energies deduced from the conductivity and electrical modulus curves are close, demonstrating that the mechanism of relaxation is the same and that the origin of relaxation may be related to the thermally activated behavior of the same charge carriers.

3.6. Adsorption studies

Selective adsorption of cationic dyes. To evaluate the properties of the free porphyrin and metalloporphyrin as adsorbents, adsorption testing was conducted with methylene blue (MB) and crystal violet (CV) as model dyes. To examine the adsorption abilities of **1** and **2** for these dyes, samples of **1** and **2** ($m = 3$ mg) were dipped into an aqueous solution of MB and CV ($C_0 = 30$ mg L^{-1}) at room temperature ($T = 298$ K), and the adsorption process was detected by UV-vis spectra (Fig. 11). After compounds **1** and **2** adsorbed the dyes, the UV spectra of the aqueous solutions showed that the characteristic peaks for MB and CV at 664 and 591 nm, respectively, decreased gradually for both compounds, indicating the removal of these dyes.

Fig. 12 shows the percentages of adsorption of MB and CV dyes on compounds **1** and **2** using MB dye as the adsorbate (Fig. 12a, black and red). For the free porphyrin, the adsorption rate was found to increase rapidly within the first 15 min and remained high up to 240 min. Similarly, for compound **2**, the adsorption rate was found to increase rapidly; however, it always remained inferior to that of the free porphyrin. In the case of CV dye as the adsorbate (Fig. 12a, blue and green), the trend of the adsorption curve was different compared to that of MB. The rate of the CV adsorption was found to be lower than MB within the first 15 min and continued to increase during the course of the reaction. The adsorption capacity was determined using eqn (8):[58]

$$q_t = (C_0 - C_t)V/m \tag{8}$$

Here, C_0 (mg L^{-1}) and C_t (mg L^{-1}) are the liquid-phase concentrations of the dye at the beginning and after equilibrium time t [min], respectively; V (L) is the volume of the solution; and m [g] is the mass of the materials used. The percentage of dye removal from aqueous solution was determined according to eqn (9):[59]

$$R\% = \left(1 - \frac{C_t}{C_0}\right) \times 100 \tag{9}$$

where C_0 = the initial concentration of dye (mg L^{-1}) and C_t = the dye concentration (mg L^{-1}) at time t.

From this equation and under the experimental conditions of room temperature, $C_0 = 30$ mg L^{-1}, $m = 3$ mg and pH 6, we found that about 42% and 44.2% of the studied dyes were removed from CV and MB, respectively, for the Co-porphyrin (**2**), while for the free porphyrin (**1**), the returns were 49.6% and 46% for MB and CV, respectively (Fig. 12b). Our porphyrin

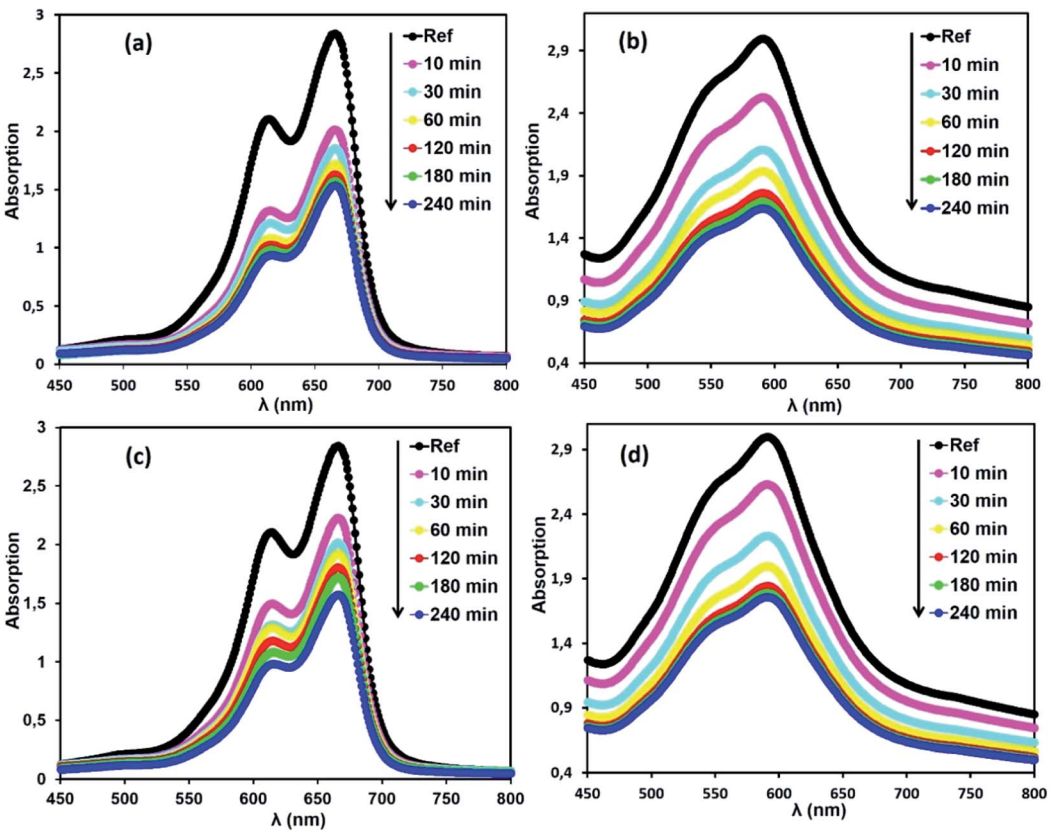

Fig. 11 Changes in the UV-vis absorption spectra of MB and CV after addition of the adsorbents, H_2TMAPP ($m = 3$ mg) [(a) and (b), respectively] and [Co^{II}(TMAPP)] ($m = 3$ mg) [(c) and (d), respectively]. The concentrations of MB and CV are $C_0 = 30$ mg L^{-1}, pH = 6 and $T = 298$ K.

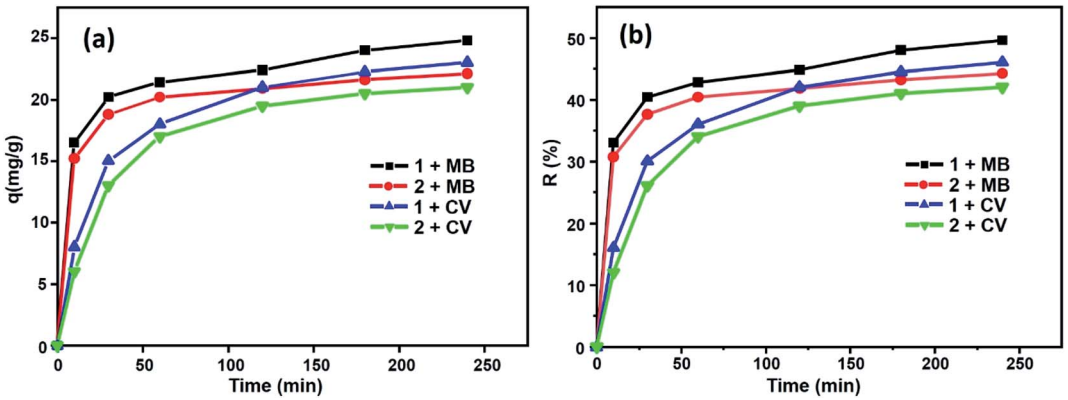

Fig. 12 Evolution of (a) the adsorption capacities for MB and CV and (b) yield removal *versus* time.

is rich in oxygen and nitrogen atoms, which aided the adsorption. Thus, intermolecular interactions occurred between the dye molecules and functional groups (oxygen and nitrogen) of the porphyrin. It is reasonable to assume that these intermolecular hydrogen bonding interactions are responsible for the selective dye adsorption, thus effectively removing MB molecules. The number of functional groups (nitrogen functions) decreased from the free to the metallated porphyrin, that is to say, when inserting cobalt into the porphyrin core.

Adsorption kinetics. The kinetics of the adsorption process is one of the most important parameters to study to evaluate the adsorption efficiency of adsorbent materials. A comparative study of the kinetics of adsorption of the two dyes MB and CV upon H_2TMAPP and [Co^{II}(TMAPP)] was performed by applying four models, including the pseudo-first-order model, pseudo-second-order model, intra-particle diffusion model, and Elovich model. The results of the fits of the experimental data are shown in Fig. 13 and Table 1.

The pseudo-first-order and pseudo-second-order kinetic models for the dyes (MB and CV) adsorbed over (**1**) and (**2**) in aqueous phases can be expressed as follows (Fig. 13a and b). By applying the pseudo-first-order model, the q_e values calculated

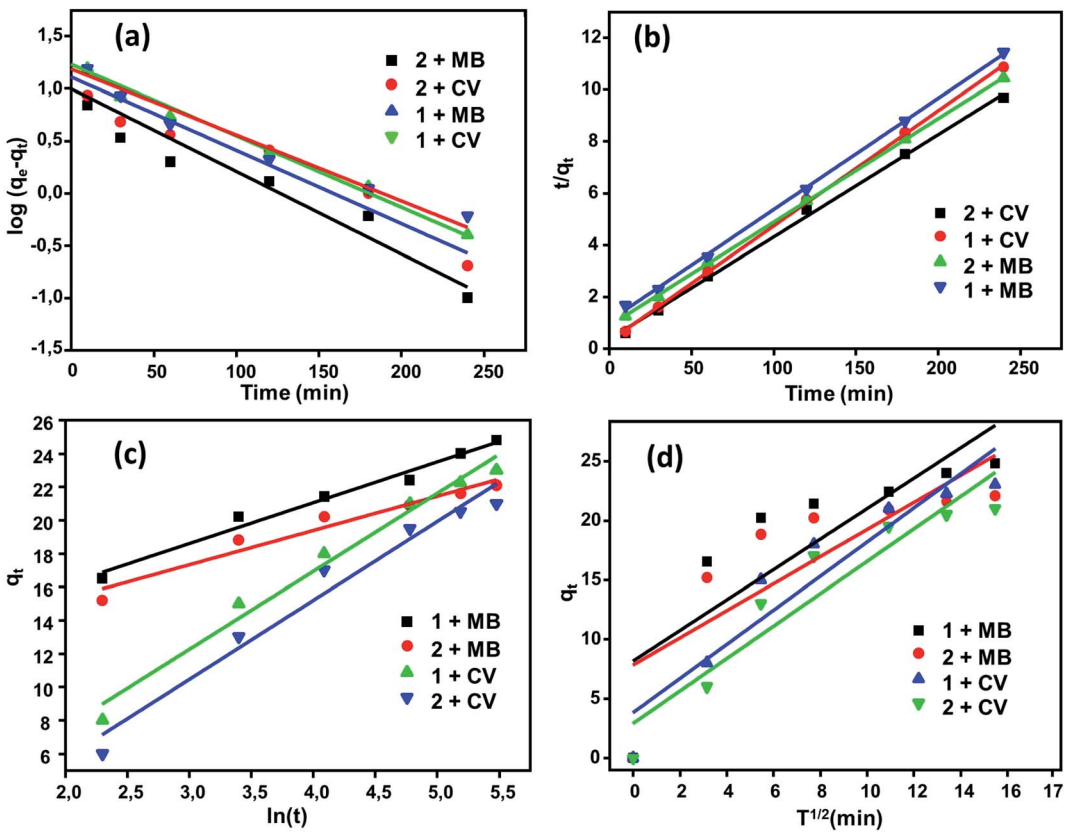

Fig. 13 Kinetic data fitted to the (a) first order and (b) pseudo-second-order equations with fitting to the models of (c) Elovich and (d) intra-particular diffusion.

 This journal is © The Royal Society of Chemistry 2020

Table 1 Kinetic data for the adsorption of MB and CV dyes using compounds **1** and **2** (C_0 = 30 mg L^{-1}, pH = 6, m = 3 mg)[a]

Kinetic equations	Calculated parameters	MB		CV	
		1	**2**	**1**	**2**
	q_{exp} (mg g^{-1})	25	22.2	23.4	21.6
Pseudo first order	k_1 (min^{-1})	0.016	0.018	0.016	0.014
	q (mg g^{-1})	12.88	9.915	17.06	15.29
	R^2	0.919	0.917	0.982	0.964
Pseudo second order	k_2 (g mg^{-1} min^{-1})	0.0043	0.0069	0.0018	0.0017
	q_{cal} (mg g^{-1})	25.31	22.47	25	23.31
	R^2	0.998	0.999	0.999	0.999
Elovich	α (mg g^{-1} min^{-1})	230.55	459.77	3.17	2.14
	β (g mg^{-1})	0.406	0.486	0.214	0.211
	R^2	0.980	0.954	0.981	0.967
Intra-particular diffusion	k_d (mg g^{-1} $min^{-1/2}$)	1.28	1.14	1.43	1.36
	R^2	0.699	0.662	0.891	0.893
	C (mg g^{-1})	8.16	7.82	3.78	2.89

[a] k_1 = the pseudo first order rate constant (min^{-1}), k_2 = the second pseudo order rate constant (g mg^{-1} min^{-1}), α (mg g^{-1} min^{-1}) = the initial adsorption rate, β (g mg^{-1}) = the desorption constant related to the extent of surface coverage and activation energy for chemisorption, k_d = the intra-particle diffusion rate constant (mg g^{-1} $min^{-1/2}$).

are smaller than the experimental q_e, and the values of the correlation coefficient [R^2 = 0.919 (H_2TMAPP), 0.917 [Co^{II}(TMAPP)] for MB and R^2 = 0.982 (H_2TMAPP), 0.964 [Co^{II}(TMAPP)] for CV] suggest that the model does not fit the adsorption process for the present porphyrin. For the pseudo-second-order model, as shown in Fig. 13b, the plots of t/q_t against t for the adsorption kinetics of MB and CV over the adsorbents H_2TMAPP and [Co^{II}(TMAPP)] gave straight lines that were well-fitted to the experimental data with high correlation coefficients [R^2 = 0.998 (H_2TMAPP), 0.999 [Co^{II}(TMAPP)] for MB and R^2 = 0.999 (H_2TMAPP), 0.999 [Co^{II}(TMAPP)] for CV], confirming a high degree of accuracy for the adsorptions. These results imply that the adsorption kinetics can be best described by a pseudo-second-order model for both H_2TMAPP and [Co^{II}(TMAPP)].

The diffusion-based model, intra-particle diffusion model and Elovich model were then fitted to determine the diffusion mechanisms of MB and CV adsorption on (**1**) and (**2**) (Fig. 13c and d). According to Table 1, the correlation coefficients for intraparticle diffusion [R^2 = 0.699 (H_2TMAPP), 0.662 [Co^{II}(TMAPP)] for MB and R^2 = 0.891 (H_2TMAPP), 0.893 [Co^{II}(TMAPP)] for CV] were lower than those for pseudo-second-order kinetics. This again suggests that the pseudo-second-order adsorption mechanism is predominant and that the overall rate of the dye adsorption process appears to be controlled by more than one step.

3.7. The catalytic degradation of methylene blue and crystal violet

Methylene blue (MB) and crystal violet (CV), two typical industrial pollutants, were chosen as model dyes to examine the catalytic behaviors of the as-synthesized Co-porphyrin. The oxidative degradation of the dyes was investigated under neutral conditions in the presence of H_2O_2 and [Co^{II}(TMAPP)] as the catalyst. Fig. 14 shows the advancement of catalytic degradation of the dyes monitored by the reduction in absorbance at the respective λ_{max} values of the dyes at different times (10, 30, 60, 120, 180 and 240 min). Fig. 15a depicts the changes in the C_t/C_0 values of MB and CV (C_0 = 30 mg L^{-1}) using different combinations. Before the degradation process, MB showed two absorption peaks centered at 664 nm (Fig. 14a). Similarly, CV exhibited two peaks at 591 nm (Fig. 14b). After the addition of H_2O_2 (6 mg L^{-1}) alone without the addition of any product, the dye solutions were stable. As [Co^{II}(TMAPP)] was added, the intensities of the peaks decreased rapidly for MB at 664 nm and for CV at 591 nm.

Moreover, the addition of this compound to the dye solutions leads to a decrease in the concentration. Using compound **2**, only 42% and 44.2% dye discoloration was achieved for CV and MB, respectively. However, using the compound **2**/H_2O_2 system (dye concentration = 30 mg L^{-1}, pH 6 and t = 4 hours of interaction), the value of the discolouration yield increased rapidly, reaching 90% for CV and 84% for MB at equilibrium. This difference in decolourisation can be explained by the fact that MB dye degrades more easily than CV. The presence of hydrogen peroxide accelerates the elimination of the dye in the solution. To this end, we proposed a catalytic mechanism based on three stages (adsorption–oxidation–desorption). The adsorption phase consists of the fixation of dyes and hydrogen peroxide on the surface of the catalyst. Hydrogen peroxide in contact with complex **2** released many more reactive hydroxyl radicals, which degrade BM and CV. Above all, it was observed that the MB and CV solutions seemed to be stable in the presence of H_2O_2 alone. These behaviors were detected when investigating the degradation of textile dyes using chitosan-supported [bis(2-methylallyl)(1,5-cyclooctadiene)ruthenium(II)].[60] According to the literature, the degradation yield of BM dye obtained using our Co(II)-porphyrin compound (84%) is comparable and in some cases even superior to those of previously synthesized and studied cobalt metalloporphyrins.[17] On the other hand, this degradation yield is lower than those obtained with metalloporphyrin polymers (99%).[61] For CV dye degradation, the yield

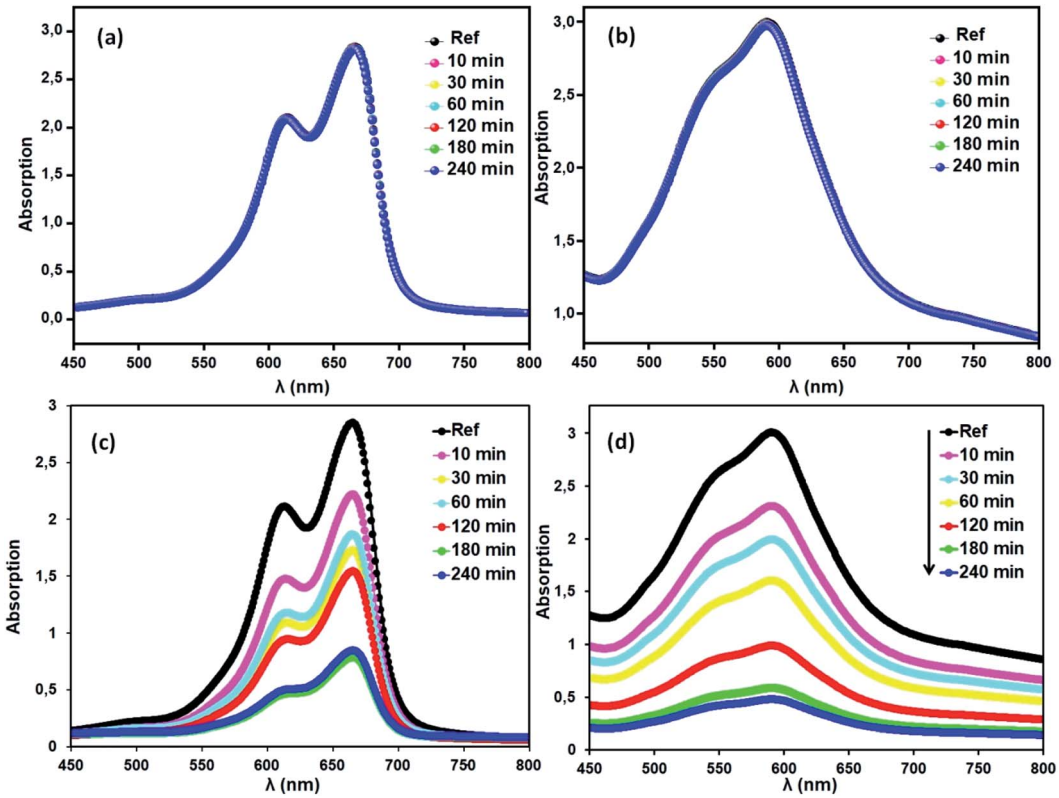

Fig. 14 Blank tests: (a) (MB), (b) (CV). Evolution of the absorbance *versus* time using the compound (**2**) (3 mg)/H_2O_2 (6 mg L^{-1}) system (c) with MB and (d) with CV. The concentrations of MB and CV were 30 mg L^{-1}, pH = 6 and T = 298 K.

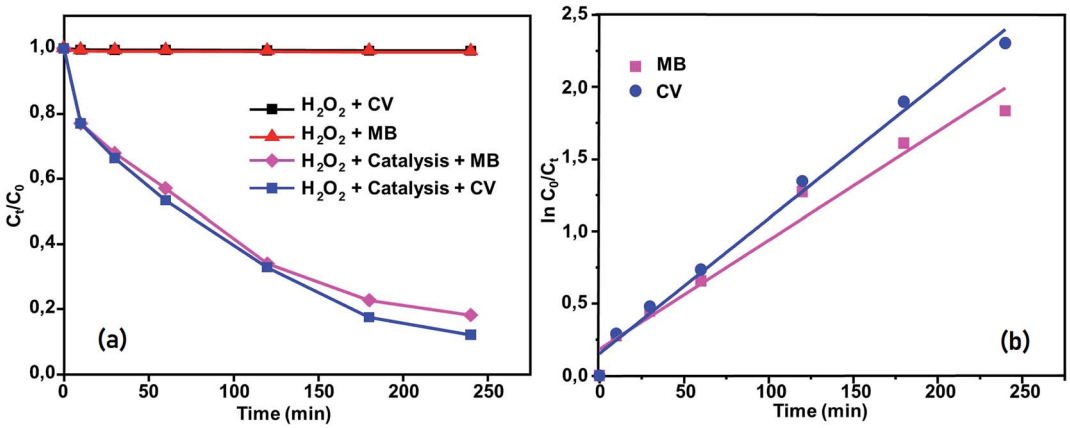

Fig. 15 (a) Changes in C_t/C_0 *versus* time for the following conditions: dyes + H_2O_2, MB + compound (**2**) + H_2O_2 and CV + compound (**2**) + H_2O_2. (b) Kinetics of [Co^{II}(TMAPP)]-catalyzed degradation of MB and CV in aqueous solution.

obtained (90%) is quite acceptable for the first reported investigation of the degradation of this dye using a porphyrin derivative.

The reactions of BM and CV solutions at 30 mg L^{-1} with hydrogen peroxide have high correlations of $R^2 = 0.98$ and $R^2 = 0.96$, respectively. This confirms that the reaction follows the pseudo-second-order kinetic model. To provide insight into the dye degradation kinetics, the constant k_0 was computed:

$$\ln\left(\frac{C_0}{C_t}\right) = k_0 t \tag{10}$$

where t is the time taken during the degradation, k_0 is the first-order rate constant of the reaction, and C_t and C_0 are the dye levels at times t and 0. As depicted in Fig. 15b, the rate constants of the degradation (k_0)[62] are 0.009 and 0.007 min^{-1} for CV and MB, respectively.

The catalyst was regenerated efficiently at the end of the catalytic process and remained stable, which was confirmed by IR (Fig. S7†), and no change was observed.

 This journal is © The Royal Society of Chemistry 2020

4. Conclusions

In summary, the synthesis and determination of the spectral and optical properties of the new porphyrin H_2TMAPP (**1**) and its cobalt complex [Co^{II}(TMAPP)] (**2**) were performed. The UV-visible spectrum of **2** exhibits a blue-shifted Soret band compared to the free porphyrin, and the fluorescence data are practically the same as those of known cobalt porphyrin complexes. The position and sharpness of the ^{1}H NMR resonances clearly demonstrate the paramagnetic nature of the complex, indicative of a Co(II) complex. The complex impedance was investigated by an equivalent circuit constituted by a resistor (R_p) in parallel with a capacitor (CPE), all in series with a resistor (R_s). The dielectric modulus confirmed the presence of a non-Debye relaxation type. The activation energies, determined from the conductivity and the electrical modulus, are comparable, which proves that the relaxation phenomenon is the same and that the origin of relaxation may be related to the thermally activated behavior of the same charge carriers. The present compounds show good adsorption properties toward two dyes (methylene blue and crystal violet) that are present in organic pollutants. The kinetic data disclosed the pseudo-second order mechanism of adsorption. Interestingly, the aggregate of [Co^{II}(TMAPP)] (**2**) exhibits higher catalytic efficiency for the degradation of cationic dyes in the presence of H_2O_2.

Conflicts of interest

There are no conflicts of interest to declare.

Acknowledgements

The Authors thank the Tunisian Ministry of Higher Education and Scientific Research for the financial support.

References

1 Z. Valicsek, O. Horváth and K. Patonaya, *J. Photochem. Photobiol., A*, 2011, **226**, 23–35.
2 S. Ahmad, R. Gautam, A. Singhal and S. M. S. Chauhan, *J. Mol. Liq.*, 2018, **260**, 292–303.
3 J. Mishra, D. S. Pattanayak, A. A. Das, D. K. Mishra, D. Rath and N. K. Sahoo, *J. Mol. Liq.*, 2019, **287**, 110821.
4 M. J. Crossley and P. L. Burn, *J. Chem. Soc., Chem. Commun.*, 1991, 1569–1571.
5 J. Kou, D. Dou and L. Yang, *Oncotarget*, 2017, **8**, 81591–81603.
6 K. Sugiyasu and M. Takeuchi, *Chem.–Eur. J.*, 2009, **15**, 6350–6362.
7 H. Song, Q. Liu and Y. Xie, *Chem. Commun.*, 2018, **54**, 1811–1824.
8 A. Ray, A. De and S. Bhattacharya, *J. Mol. Liq.*, 2017, **246**, 17–24.
9 S. M. Shaikh, A. Chakraborty, J. Alatis, M. Caia, E. Danilov and A. J. Morris, *Faraday Discuss.*, 2019, **216**, 174–190.
10 C. W. Leishman and J. L. McHale, *J. Phys. Chem. C*, 2015, **119**, 28167–28181.
11 J. Otsuki, *J. Mater. Chem. A*, 2018, **6**, 6710–6753.
12 O. Oviedo, T. Zoltan, F. Vargas, I. Marcel and J. C. Vivas, *J. Coord. Chem.*, 2014, **67**, 1715–1730.
13 D. M. Carminati, D. Intrieri, S. Le Gac, T. Roisnel, B. Boitrel, L. Toma, L. Legnanic and E. Galloa, *New J. Chem.*, 2017, **41**, 5950–5959.
14 M. F. Isaac and S. B. Kahl, *J. Organomet. Chem.*, 2003, **680**, 232–243.
15 D. Mohajer, G. Karimipour and M. Bagherzadeh, *New J. Chem.*, 2004, **28**, 740–747.
16 G. Karimipour, B. Karami, M. Montazerozohori and S. Zakavi, *Chin. J. Catal.*, 2007, **28**, 940–946.
17 M. Guergueb, S. Nasri, J. Brahmi, F. Loiseau, F. Molton, T. Roisnel, V. Guerineau, I. Turowska-Tyrk, K. Aouadi and H. Nasri, *RSC Adv.*, 2020, **10**, 6900–6918.
18 N. Amiri, S. Nouir, M. Hajji, T. Roisnel, T. Guerfel, G. Simonneaux and H. Nasri, *J. Saudi Chem. Soc.*, 2019, **23**, 781–794.
19 N. Amiri, M. Hajji, F. Ben Taheur, S. Chevreux, T. Roisnel, G. Lemercier and H. Nasri, *J. Solid State Chem.*, 2018, **258**, 477–484.
20 R. Soury, M. Jabli, T. A. Saleh, W. S. Abdul-Hassan, E. Saint-Aman, F. Loiseau, C. Philouze and H. Nasri, *RSC Adv.*, 2018, **8**, 20143–20156.
21 D. D. Perrin and W. L. F. Armarego, *Purification of Organic Solvents*, Pergamon Press, Oxford, 1988.
22 V. S. Sharma, A. S. Sharma, R. H. Vekariya and R. B. Patel, *Mol. Cryst. Liq. Cryst.*, 2017, **658**, 32–44.
23 J. S. Lindsey, H. C. Hsu and I. C. Schreiman, *Tetrahedron Lett.*, 1986, **27**, 4969–4970.
24 A. D. Adler, F. R. Longo, F. Kampas and J. Kim, *J. Inorg. Nucl. Chem.*, 1970, **32**, 2445–2448.
25 C. A. Pessoa and Y. Gushikem, *J. Porphyrins Phthalocyanines*, 2001, **5**, 537–544.
26 S. Forgues and D. Lavabre, *J. Chem. Educ.*, 1999, **76**, 1260.
27 M. D. Maree, T. Nyokong, K. Suhling and D. Phillips, *J. Porphyrins Phthalocyanines*, 2002, **6**, 373–376.
28 K. Ezzayani, A. Ben Khelifa, E. Saint-Aman, F. Loiseau and H. Nasri, *J. Mol. Struct.*, 2017, **1137**, 412–418.
29 R. Farran, D. Jouvenot, F. Loiseau, J. Chauvin and A. Deronzier, *Dalton Trans.*, 2014, **43**, 12156.
30 A. Mansour, Y. Belghith, M. S. Belkhiria, A. Bujaczb, V. Guérineau and H. Nasri, *J. Porphyrins Phthalocyanines*, 2013, **17**, 1094–1103.
31 A. M. Shaffer and M. Gouterman, *Theor. Chim. Acta*, 1972, **25**, 62–82.
32 M. Gouterman, *J. Chem. Phys.*, 1959, **30**, 1139.
33 D. M. Lyons, J. Kesters, W. Maes, W. Christopher, J. Bielawski and L. Sessler, *Synth. Met.*, 2013, **178**, 56–61.
34 K. Ezzayani, A. Ben Khelifa, E. Saint-Aman, F. Loiseau and H. Nasri, *Polyhedron*, 2016, **117**, 817–825.
35 B. Yan, X. Liu, T. Ghugare, N. Fedorka and Y. F. Li, *J. Coord. Chem.*, 2015, **68**, 2827–2834.
36 W. Chen and S. Fukuzumi, *Eur. J. Inorg. Chem.*, 2009, 5494–5505.
37 Y. X. Du, Z. Q. Zhang, Y. H. Yao and J. Li, *Inorg. Chem. Commun.*, 2016, **64**, 19–22.

38 J. Patwari, A. Chatterjee, S. Sardar, P. Lemmens and S. K. Pal, *Phys. Chem. Chem. Phys.*, 2018, **20**, 10418–10429.

39 K. M. Kadish and M. M. Morrison, *J. Am. Chem. Soc.*, 1976, **98**, 3326–3328.

40 X. Ke, R. Kumar, M. Sankar and K. M. Kadish, *Inorg. Chem.*, 2018, **57**, 1490–1503.

41 K. M. Kadish, X. H. Mu and X. Q. Lin, *Inorg. Chem.*, 1988, **27**, 1489–1492.

42 L. A. Truxillo and D. G. Davis, *Anal. Chem.*, 1975, **47**, 2260–2267.

43 C. Paul-Roth, J. Rault-Berthelot, G. Simonneaux, C. Poriel, M. Abdalilah and J. Letessier, *J. Electroanal. Chem.*, 2006, **597**, 19–27.

44 M. M. El-Nahassa, H. S. Metwallya, H. E. A. El-Sayeda and A. M. Hassaniena, *Mater. Chem. Phys.*, 2012, **133**, 649–654.

45 A. Badri, M. Jabli, M. L. López and M. Ben Amara, *Inorg. Chem. Commun.*, 2019, **110**, 107609.

46 M. S. Masoud, A. E. Ali, M. A. E.-Z. Mostafa and R. H. Mohamed, *Spectrochim. Acta, Part A*, 2005, **62**, 1114–1119.

47 S. G. Kakade, Y.-R. Ma, R. S. Devan, Y. D. Kolekar and C. V. Ramana, *J. Phys. Chem. C*, 2016, **120**, 5682–5693.

48 A. K. Jonscher, *Nature*, 1977, **267**, 673–679.

49 S. R. Elliott, *Adv. Phys.*, 1987, **36**, 135–218.

50 M. M. Shehata, T. G. Abdel-Malik and K. Abdelhady, *J. Alloys Compd.*, 2018, **736**, 225–235.

51 M. M. El-Nahass, H. M. Zeyada and M. M. Makhlouf, *Appl. Phys.*, 2011, **11**, 1326–1331.

52 T. Ceyhan, A. Altındal, M. K. Erbil and Ö. Bekaroglu, *Polyhedron*, 2006, **25**, 737–746.

53 R. Ranjan, R. Kumar, N. Kumar, B. Behera and R. N. P. Choudhary, *J. Alloys Compd.*, 2011, **509**, 6388–6394, DOI: 10.1016/j.jallcom.2011.03.003.

54 I. M. Afandiyeva, I. Dökme, S. Altındal, M. M. Bülbül and A. Tataro glu, *Microelectron. Eng.*, 2008, **85**, 247–252.

55 S. B. Aziz and Z. H. Z. Abidin, *J. Appl. Polym. Sci.*, 2015, **132**, 41774.

56 S. R. Elliott, *Solid State Ionics*, 1988, **27**, 131–149.

57 M. M. El-Nahass, A. A. M. Farag, F. S. H. Abu-Samaha and E. Elesh, *Vacuum*, 2014, **99**, 153–159.

58 L.-L. Lv, J. Yang, H.-M. Zhang, Y.-Y. Liu and J.-F. Ma, *Inorg. Chem.*, 2015, **54**, 1744–1755.

59 M. S. Khan, M. Khalid, M. S. Ahmad, M. Shahid and M. Ahmad, *Dalton Trans.*, 2019, **48**, 12918.

60 M. Jabli, R. Touati, Y. Kacem and B. B. Hassine, *J. Text. Inst.*, 2012, **103**, 434–450.

61 Y. Li, L. Wang, Y. Gao, W. Yang, Y. Li and C. Guo, *RSC Adv.*, 2018, **8**, 7330.

62 V. S. Sharma, A. S. Sharma, R. H. Vekariya and R. B. Patel, *Mol. Cryst. Liq. Cryst.*, 2017, **658**, 32–44.

 This journal is © The Royal Society of Chemistry 2020